Fluid flow measurements in fully penetrated 316L TIG welding

Nicolas Blanc, Fabien Soulié, Issam Bendaoud, Sébastien Rouquette, Frédéric Deschaux-Beaume, Cyril Bordreuil

Fluid flow measurements in fully penetrated 316L TIG welding

Nicolas Blanc[1] · Fabien Soulié[1] · Issam Bendaoud[1] · Sebastien Rouquette[1] · Frédéric Deschaux-Baume[1] · Cyril Bordreuil[1]

Abstract
Fluid flow motion controls energy transfer in the weld pool and drives solidification process. Experimental investigation of fluid flow during welding is made particularly difficult by unsteady movements in the molten pool. Fluid flow measurements in tungsten inert gas (TIG) welding are important to understand and control energy transfers during the process. In this paper, a setup was designed to observe free surfaces during a fully penetrated TIG welding. Edge detection is applied to obtain the weld pool border, and particle tracking velocimetry (PTV) method is applied based on gas bubbles and particles along the free surface opposite to the arc. The method allows to investigate velocities and fluid flow motion. The method is carried on three different welding speeds at a constant current (80 A) leading to three different linear heat inputs. Images on the penetrated side showed oscillations of the fluid flow that goes from one vortex on the side of the weld pool to the other vortex on the other side. Velocity measurements can give insight to the intensity of the fluid flow. Finally, its behavior are discussed in relation with assumption of its 3D component and its physical origin.

Keywords Welding · Weld pool · Fluid flow · Particle tracking velocimetry · 316L

1 Introduction

Arc welding is widely used in aerospace, automotive and power generation industries, and is used to join two metallic parts with a localized energy density. A heat input initiates complex physical and chemical processes, namely metal melting and solidification or fluid flow and vaporization. The final geometry of the weld and its metallurgical structure are controlled by heat transfer in the molten pool. Understanding the distribution of temperatures in the weld pool is then important for assessing the quality of welded joints. Finding process parameters which insure temperature homogeneity inside the weld pool is then very important for welders, and due to the physics, fluid motion plays an important role in this distribution. Fluid flow is driven by different forces acting in the liquid metal or at the weld pool surface and is highly coupled to thermal field. Buoyancy forces, Lorentz forces, shear stresses induced by the arc plasma, arc pressure, and Marangoni stresses drive complex fluid flow inside the weld pool [1, 2]. Depending on the material properties (sulfur content or other surface active elements) [3], the welding technology, the process parameters [4], and the moment during the welding process when the molten pool is observed [5], the different forces do not have the same intensity, but Marangoni force is often considered to be one of the most important. In that context, numerical modeling is useful to better understand the respective influences of these forces [6–10], but it is still computing intensive and experimental data are often required to be compared for validation of the assumptions of the modeling.

Experimental procedures to observe the weld pool and its fluid flows have been developed over the years. Traditional high speed cameras can be embedded to monitor the process, and different algorithms can then be used to catch coherent structures of the fluid flow. Several authors have observed in the literature complex fluid flows inside TIG welding pools. Zhao et al. [11] have used particle image velocimetry (PIV)

✉ Nicolas Blanc
nicolas.blanc111@gmail.com

Fabien Soulié
fabien.soulie@umontpellier.fr

[1] LMGC, University Montpellier, CNRS, Montpellier, France

for applications on 316L steel by tracking natural oxide particles. They have observed outwards and rotational flows with the formation of vortexes with a mean fluid velocity between 50 and 100 mm/s. In another study of Zhao et al. [12], inward flows have been observed with a velocity around 300 mm/s. This flow is commonly attributed to a positive surface tension gradient. With this kind of velocities, the Reynolds number was between 600 and 3000 and showed multiple cells. Chiocca et al. [13] have observed on fused Cu30Ni fully penetrated weld pool two vortexes on both sides of the pool and on each side of the plate with the presence of a backward flow. Using a PTV method, they could measure a frontward flow coming from the solidification zone with a mean fluid velocity around 120 mm/s. At this velocity, the Reynolds number is around 2000 with their process parameters. These values of Reynolds number mean that the turbulence can appear, and it is known that it drastically modifies the heat transfer [14]. X-ray transmission observations of internal flows are also possible in welding in 2D [5, 15–17] or in 3D [18, 19]. This kind of measurement showed the importance of convective flow for heat transport with high fluid flow velocities in PKAW [19] and that it influenced strongly spatter and other defect formation in laser welding [15, 18]. Although it gives access to inaccessible details otherwise, these techniques remain heavy compared to traditional camera surface observations and are restricted to lab experiments.

One objective of this paper is to contribute to the understanding of physics inside the weld pool with devices that can be embedded during the process. The originality comes from the combination of a macroscopic measurement with a local measurement. The global measurement uses edge detection to determine the size and the shape of the weld pool, whereas the local measurement uses particle tracking velocimetry to estimate fluid velocity inside the liquid metal. Another originality comes from the particular setup used and from the fully penetrated weld pool on 316L. These measurements can also serve as a benchmark for simulations.

The first section of this study describes the material and methods used to observe and measure the flow existing at the weld pool surface. The second section presents qualitatively and quantitatively the movements of the fluid. The third section discusses the results and their influence on the physical phenomenon.

2 Materials and methods

2.1 Material

The chemical composition of the 316L stainless steel used in this study is resumed in Table 1.

The values of the density ρ, superficial tension σ, and viscosity μ used are listed in Table 2.

2.2 Experimental setup

A schematic diagram of the experiment is presented in Fig. 1. The set-up consists of a TIG torch, a 1.5 mm thick plate, and two cameras which are fixed with respect to the torch.

A 2.4 mm diameter tungsten electrode with 2 % lanthanum, with a 30 degrees grinding angle, is positioned 3 mm away from the sample during welding and is kept fixed. A 28.6 mm diameter nozzle releases pure argon at 15 L/min to shield the liquid metal on the arc side. The 316L stainless steel plate is clamped on a guided motorized stand to produce a bead on plate with a fully penetrated weld pool. An independent flow of argon fills a chamber underneath the plate (shown in purple in Fig. 1) in order to purge oxygen and protect the weld pool from oxidation.

The arc is initiated by lift-arc procedure at the beginning of the experiment, and the table begins to move 0.4 s after arc initiation. The plate travels a distance of 100 mm. We chose to perform three different experimental tests, with three different welding speeds w_s of 2.3, 3.3, and 4.3 mm/s. The welding current was kept at 80 A. These conditions create a fully penetrated weld pool. These three welding speeds are chosen in order to modify only one process parameter and to vary consequently the linear heat input. By changing the welding speed, the weld pool is expected to have different sizes and shapes. It is also expected that changing velocity will change the flow structure inside the weld pool. Arc voltage and current are measured with an acquisition rate of 10 kHz.

The energy delivered by the welding station is monitored by measuring the electric current I thanks to a current sensor and by measuring the arc voltage U between the ground and the electrode holder. The average of these two measurements

Table 1 Chemical composition (in percent) of 316L stainless steel

Component	C	Cr	Mn	Mo	Ni	P	S	Si	N	Co
Ratio	0.016	16.765	1.383	2.044	10.070	0.031	0.001	0.389	0.041	0.187

Table 2 Density, surface tension and viscosity of 316L stainless steel at 1925 K (literature data)

Property (unit)	Value	Reference
ρ (kg.m^{-3})	6774	[20]
σ (N.m^{-1})	1.77	[21]
μ (Pa.s)	6.36×10^{-3}	[22]

Table 3 Mean current, arc voltage, and linear energy for the three different welding speeds

w_s (mm/s)	I (A)	U (V)	E_l (J/mm)
2.3	81.7	8.58	305
3.3	81.3	8.76	216
4.3	81.5	8.67	164

is resumed in Table 3 for the three different welding speeds w_s. It allows the linear energy $E_l = \frac{UI}{w_s}$ to be computed (heat input per unit length of weld bead, see Table 3). The linear energy is multiplied by two between the lowest and the highest.

Because 3D flow can be very complex to observe [19], we decided to observe the liquid metal along free surfaces in a fully penetrated weld bead on a thin plate.

The weld pool surfaces are observed by cameras (Mako, Allied Vision Technologies) at 300 frames per second (Fig. 1) with a resolution of 640x480 px on the side of the arc and a 800x600 px at the bottom of the plate. A frame rate of 300 Hz is set to the cameras and is fixed by an external counter insuring the synchronization of images.

Figure 2a shows an image on the upper face of the plate, on the side of the arc. The liquid metal and part of the solid plate can be clearly distinguished. A large white (saturated) region inside the weld pool corresponds to the reflection of the arc and the electrode. It partially hides information in the weld pool.

As the other camera is placed below the plate, there is no perturbation due to the light emitted by the arc (Fig. 2b). Due to the geometry of the stand supporting the plate, the first 30 mm of weld bead is not visible from the camera placed below the stand.

In Fig. 2b, the texture in the liquid metal is smooth. Small white disks of different sizes are visible on the surface of the melt pool. The white disk at the bottom of the image at the lower side is a bubble, and it will be used as a tracer in the particle tracking velocimetry algorithm. By comparison, the solid part appears darker, and its texture is revealed by speckle created by the reflection of a 808 nm diode laser's low-angled light at a power of 15 W on solidified surface. Equipped with a collimator, the width of the light beam is approximately equals to the width of the metal plate. This input power is low and is not modifying heat input, as an experience without this laser showed exactly the same behavior.

For Fig. 2b, some regions of the weld pool appear brighter than others. These regions have a high temperature, and the radiance of the surface is greater than the one of colder regions. The camera sensor received then more luminous flux.

2.3 Image processing

In this part, the details to measure length on images are explained. As shown in Fig. 1, the cameras are tilted, and so a calibration procedure is applied to correct the image in the plane of the plate. At the end, the images are transformed in the same way as calibration chessboard (see [23]). This pro-

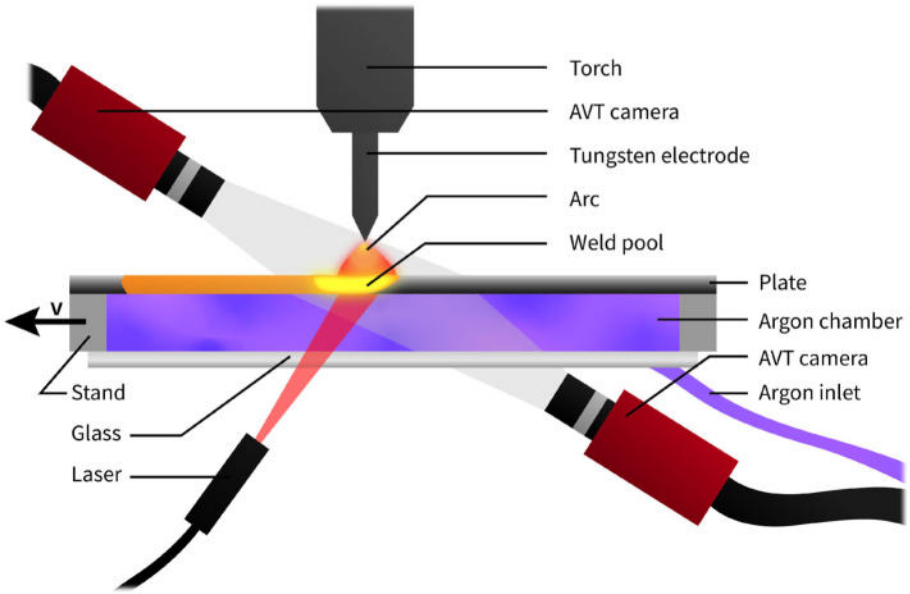

Fig. 1 Diagram of the experimental set-up

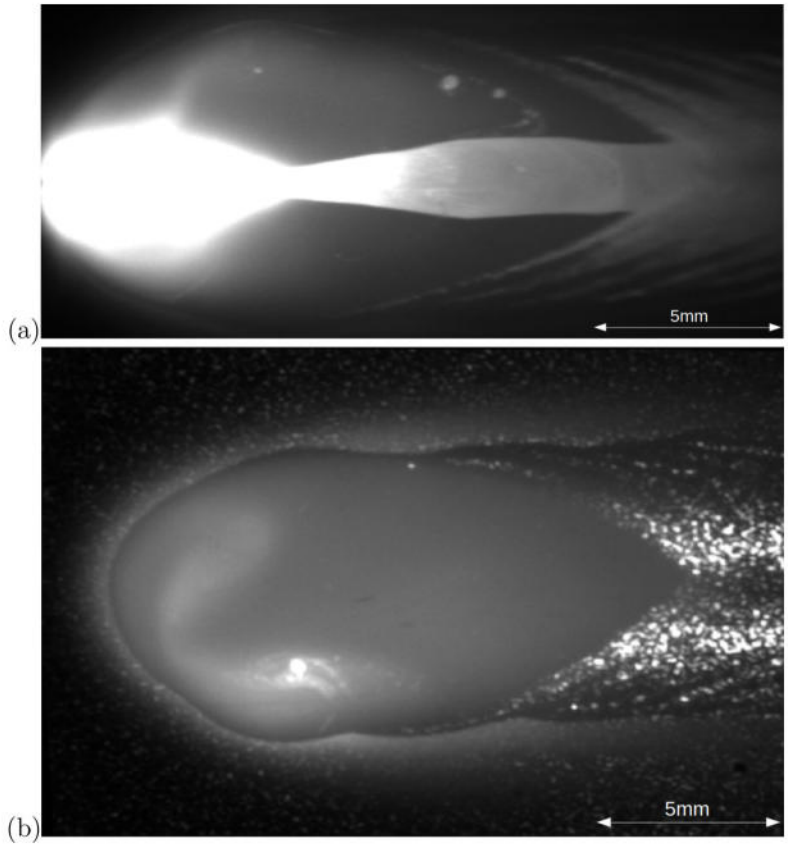

Fig. 2 Example of the images of the weld pool captured above the plate (**a**) and below (**b**) with w_s =2.3mm/s

cedure allows us to also obtain the scale of the images and to measure length. The precision can be estimated around 50 μm.

Due to the presence of the arc, the images from the top are only used for qualitative information.

A program was implemented for edge detection to have the geometry of the weld pool at the bottom surface. This process consists of several steps: *(i)* using template matching to separate region of different textures (fluid and solid), *(ii)* using a Canny filter to separate regions, and finally *(iii)* using alpha shape algorithm to link points. If necessary, the different contours (linked points) found by the algorithm can be filtered with their area or their length.

The different steps of the algorithm are shown in Fig. 3.

The final processed image is shown in Fig. 3d. The contour matches the border of the weld pool within one or two pixels. The procedure is used for each image of the weld bead. It is robust because more than 90% of weld pool borders are detected. It means that the geometry (surface, shape) of the weld pool can be monitored all along the process.

2.4 Particle tracking velocimetry

The presence of bubbles and oxide particles at the surface of the weld pool allows to track them and measure the speed flows. Usually, only one or two tracers are detected simultaneously, usually with a spherical shape indicating mostly that it is a bubble (Fig. 2b, for example).

To begin, the relevance of measuring the particle motion to obtain fluid flow is discussed. Depending on the characteristics of the particle or the bubbles, their velocity can be significantly smaller than the velocity of the flow of the liquid near the free surface. To estimate this possible difference of velocity, different dimensional numbers can be calculated. The Stokes number (Stk) is generally computed for suspension to appreciate their drag in the bulk. In our case, bubbles and particles are wetting on the free surface. The capacity of the flow to drag the bubbles or the particles can be more appreciated by the Capillary number:

$$C_a = \frac{\mu V}{\sigma} \tag{1}$$

With a velocity V approximating $1\, m.s^{-1}$ and the material parameters given, the capillary number is lower than 10^{-1}, revealing that surface tension is the dominant effect acting on the bubble or particle. This indicates that the bubble can follow the bulk flow. Nevertheless, bubbles may not follow exactly the fluid motion because of slipping between the liquid and the object being tracked. We have to consider the

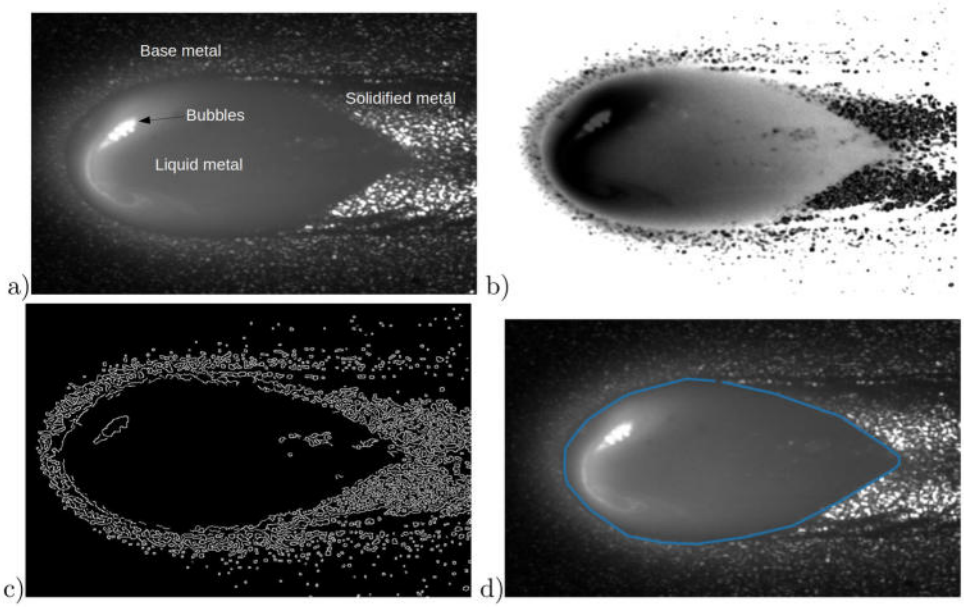

Fig. 3 View of the bottom side of the weld pool (**a**) with *template matching* filter (**b**), then Canny filter (**c**), and the final contour detection with *alpha shapes* (**d**)

measured velocity of the bubble as a lower bound of the real fluid velocity.

The particle velocity is measured by applying the PTV method using the Trackpy library [24]. The algorithm identifies the brightness peak corresponding to the particles or bubbles floating on the surface on one image. The algorithm tracks then the peak and creates a parent-child couple of particle between each images in the flow. The algorithm gives then the position of the center of the particle on each image and builds a trajectory. Sometimes, particle disappears due to a change of brightness or due to fusion. In that case, it can interrupt the trajectory building, leading the algorithm to create a new one once the tracer is back. The uncertainties are due to bad positions if similar particles are present in the images. In this experiment, one or two particles clearly different from the others are detected, leading to few mistakes. Moreover, the distortions are sufficiently small to not introduce a bad position of the center of the particle. The results of the PTV algorithm (x and y coordinates of the peaks) are visible in Fig. 4. A spatial filter is applied in order to smooth the trajectory (curve filter in Fig. 4).

The curvilinear abscissa along the trajectories is then computed. The speed u_i of the particle at time t_i is then calculated by a simple explicit formula:

$$u_i = \frac{s_{i+1} - s_i}{t_{i+1} - t_i} \tag{2}$$

with s_i the curvilinear abscissa of the particle at time t_i. Considering the spatial resolution of 25 µm/pixel and the temporal resolution, the minimum instantaneous velocity that we can measure is equal to 7.5 mm.s^{-1}. If the measured maximum speed is higher than this lower limit, then we can consider it valid.

3 Results

First, the modification of the process parameters is shown in order to quantify its effect on the macroscopic scale. In a second step, fluid flows are analyzed based on videos to see the flow structures. Then, with the trajectories computed with PTV, the velocities can quantify the local effect inside the weld pool.

3.1 Weld pool geometry

Based on the image processing, the weld pool is recorded, and a contour is extracted on each image on the bottom side of the plate. The weld pool area is measured along the weld bead for the three different process parameters (Fig. 5).

As expected, the weld pool size increases with the linear energy input. For weld bead lower than 60 mm after initiation, some variations of the weld pool size can be seen. It is due to the fact that the weld pool is not fully settled. For distances higher than 60 mm, the variations are less significant,

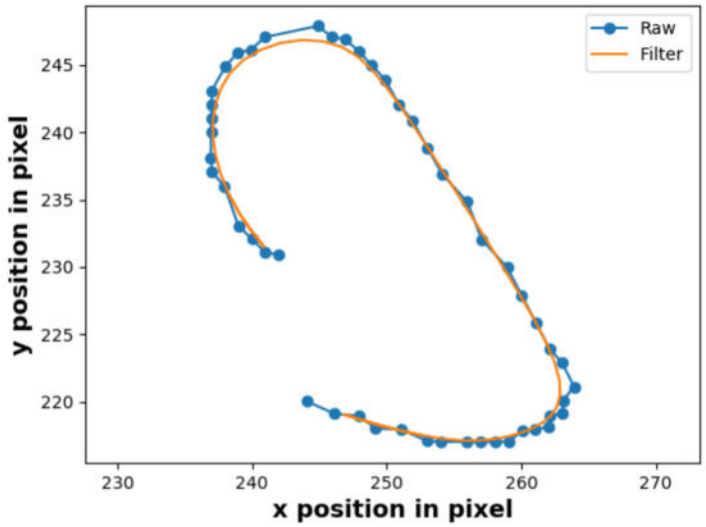

Fig. 4 Raw positions of a particle computed by the PTV algorithm and the filtered trajectory

traducing a stable regime for the weld pool. All the characteristics of weld pool and fluid flows are determined during this stable regime. The results of Fig. 5 indicate that more the linear heat input is high (low velocity), more the contour has variation. This fluctuation can come from the difficulty to detect the weld pool border with the edge detection procedure, but the analysis of the obtained contours shows a good approximation with the images. In fact, the fluctuations are only due to the change of the weld pool borders during the welding.

Figure 6 shows the detected mean contours for the three different welding speeds, with a global shape mixing elliptical and teardrop shapes. The elongation of the weld pool increases with the welding speed w_s, with a ratio length to width higher than 2 (see Table 4). The results are in agreement with simulation results where the power input ($U \times I$) is constant and only the velocity is changed.

It is important to notice at this stage the change of width relative to welding velocity. It is known that there is a non-linear relationship between the width of the weld pool and the linear heat input [25].

3.2 Fluid flow description

The PTV method allows the fluid flows to be described and the associated speeds to be computed with Eq. 2. Table 5 presents the mean and maximum speeds of tracers (bubbles or particles) detected on videos for the three different process parameter configurations. We can clearly note an increase of velocities magnitude with the linear heat input. Examples of images used for each welding speed with and without marker

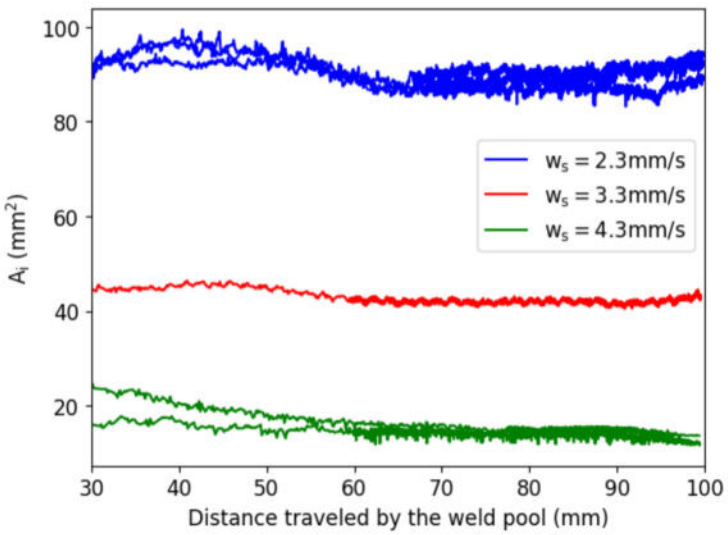

Fig. 5 Area of the weld pool on the bottom side of the weld pool along the weld bead length

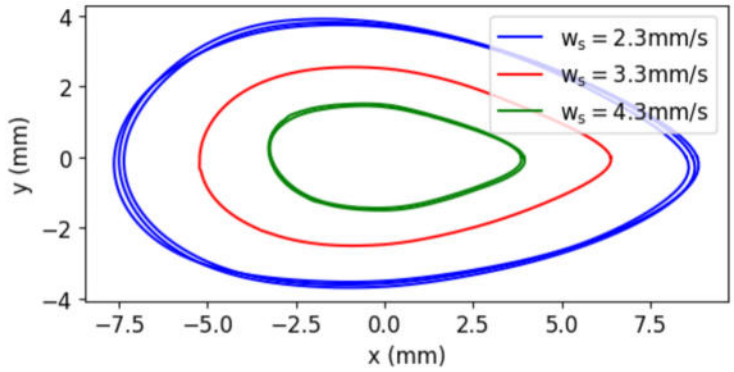

Fig. 6 Mean contour of the different weld pools in the quasi-constant phase

surrounding the particles being tracked are available in the supplementary material. In the next sections, PTV results are analyzed independently for each welding speed.

Considering these values of maximum speed, our spatial and temporal resolutions, we can compute that between each frame, the displacement of the tracer is equal to 21.7, 4.5, and 2.5 pixels for w_s, which equals to 2.3, 3.3, and 4.3 mm.s^{-1}, respectively. We can then consider the maximum speed measured for the two lower welding speeds as accurate. For the highest welding speed however, we should consider the maximum velocity as a lower bond, although the pseudo sinusoidal movement we detected for this test is quiet well determined with our set-up (Fig. 4).

3.2.1 Low welding speed $w_s = 2.3$ mm/s

On the top side of the weld pool, observations of fluid flows revealed two rotational movements (vortex), simultaneously on both sides of the weld pool and directed outwards (Fig. 7). As tracers are not always present or visible due to the presence of the arc and its reflection, the velocity of the flow and the continuity of presence of these vortexes cannot be determine. But the presence of these vortexes is in accordance with the observations of Chiocca et al. [13] that described the supposed inward and backward flows.

When focusing on the gray levels of pictures, fluctuations of the mean value can be noticed, switching from one side of the weld pool to the other (Fig. 7). These fluctuations are regular, leading to an oscillating behavior from one side of the weld pool to the other. Assuming that gray level variation is due to spectral radiation variation and then to temperature variation according to Planck's law, we can assume that variation of gray level is due to temperature variation; the higher levels of gray corresponding to the higher temperatures. The oscillating behavior reveals then that the amount of heat carried by the flow is oscillating, alternatively being higher on each side of the weld pool. It can be seen that the border of the weld pool changes with this oscillation behavior inside the liquid metal.

On the bottom side of the weld pool, only one outward vortex is observable at a time. It is located in the front part of the weld pool and on one side relatively to the weld pool axis (Fig. 8). Most of the visible tracers are located in this vortex.

Regularly, we can note a change of the side where the vortex is observed. The initial vortex disappears, and a liquid flow moves the particles to the other side, leading to the initiation of a new vortex (Fig. 8). Simultaneously, we can note variation in gray levels traducing the existence of a hot flow in the front part of the weld pool. Shortly after the new vortex is established, a significant increase of gray levels is observed in its location.

Figure 9 compares mean gray level on the left side for the two sides of the plates.

This increase is concomitant with reaching the maximum level of gray next to the arc on the top side of the weld pool (Fig. 9). This phenomenon repeats at a frequency of approximately 0.9 Hz.

Table 4 Mean length (L) and width (W) of the weld pool on the bottom side of the plate

w_s (mm/s)	W (mm)	L (mm)	L/W
2.3	7.39	16.3	2.21
3.3	5.01	11.7	2.34
4.3	2.86	7.13	2.49

Table 5 Mean and maximum speed of the tracers on the bottom side of the weld pool

w_s (mm/s)	2.3	3.3	4.3
Mean speed (mm/s)	39.3	13.6	5.2
Maximum speed (mm/s)	163.5	34.4	18.5

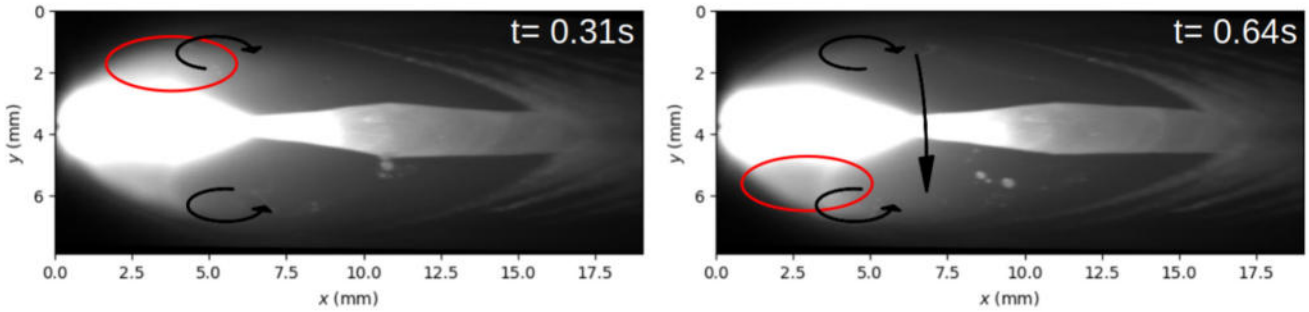

Fig. 7 Movement of the liquid metal on the top side of weld pool for $w_s = 2.3$ mm/s, at two different times. Arrows represent the visible movement of the fluid, and the gray level increase on each side of the arc is circled in red

The alternate circulation of liquid metal leads to a slight asymmetrical melting of metal in the fusion front. Consequently, the weld pool is globally oscillating around the welding torch trajectory at the same frequency as the fluid flow as shown in Fig. 10.

As observed for $w_s = 2.3$ mm/s configuration, a similar oscillating behavior between the two vortexes exists with liquid moving from one side to the other. With the same type of graph as Fig. 9, it can be observed a frequency of around 0.55 Hz.

3.2.2 Medium welding speed $w_s = 3.3$ mm/s

Because of the absence of visible tracers on the front side of the weld pool, no liquid movement is observed on this side at this welding speed. On the bottom side, two vortexes are observed, located on each side of the weld pool (Fig. 11). They are spinning from the rear to the front of the weld pool in outward movements.

3.2.3 High welding speed $w_s = 4.3$ mm/s

At $w_s = 4.3$ mm/s, the weld pool is slightly asymmetric with only one vortex visible on one side on the bottom side of the weld pool (Fig. 12).

A smaller one is sometimes visible on the other side, but no particle is observed and the measurement of the velocity

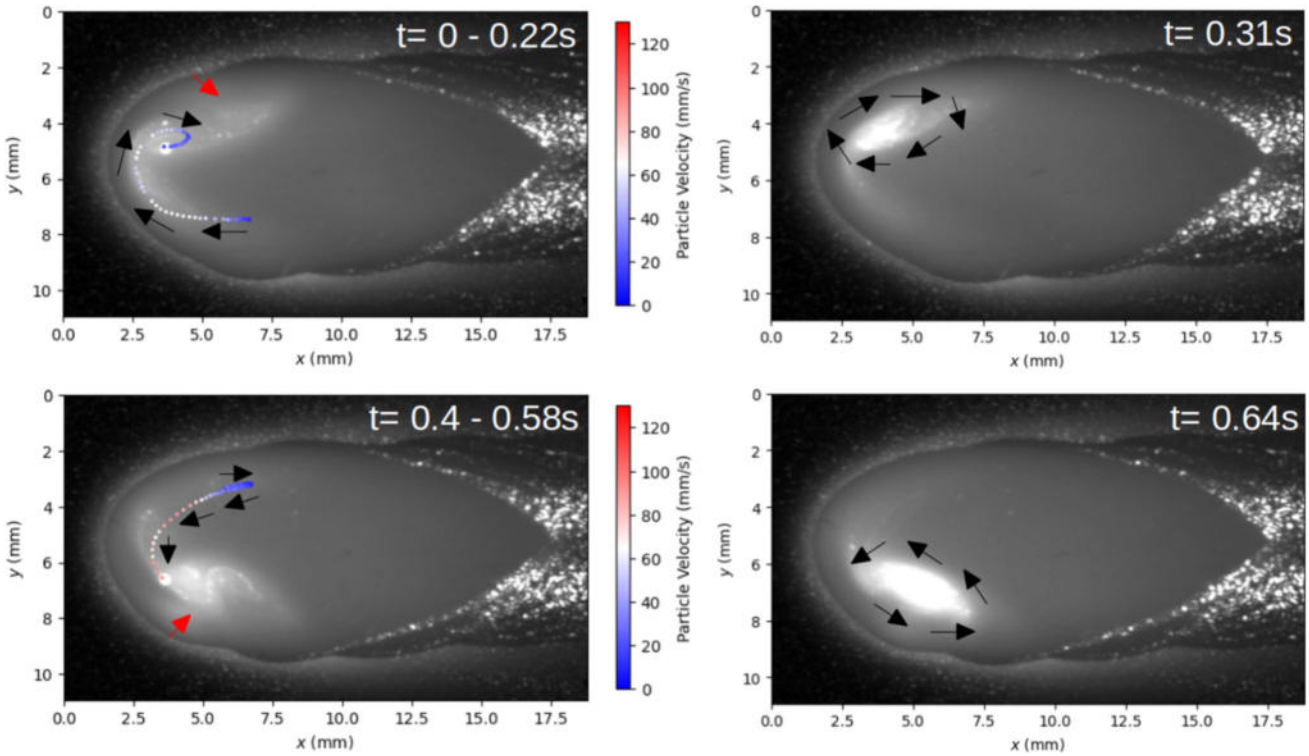

Fig. 8 Oscillating movement of the particles for $w_s = 2.3$ mm/s, bottom side. The black arrows show the way the particle is moving. The red arrows represent hot flows

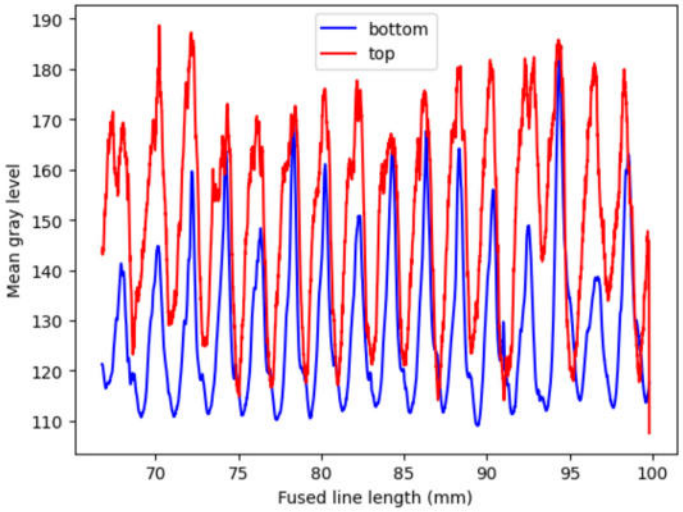

Fig. 9 Mean gray value on the left side (in the welding direction) of the fused metal on each side of the plate

inside this vortex by the PTV algorithm is not possible. On the upper side of the weld pool, no liquid motion is visible.

4 Discussion

The different observations allow a better understanding of the liquid movements of the weld pool, at least on the surfaces.

The results obtained clearly show a logical increase of the size of the weld pool in direct relation with the increase of linear energy due to the decrease of welding speed. On the bottom side of the weld pool, fluid particle velocity measurements also show an increase in surface liquid velocities (average and maximum observed) with increasing linear energy. The fact that the mean velocities measured are lower than the results of the literature for top surface velocity is in accordance with what shown by Ebrahimi et al. [7], as they observed an outward flow at the top surface and low velocity on the bottom surface for low sulfur content. The fluid velocity being higher for the lowest welding speed can be explained by the fact that the length on which is acting the Marangoni shear force (see discussion in the next paragraph) is higher with a larger weld pool. Ebrahimi et al. [7] also numerically predict an oscillating behavior inside the weld pool with their simulations.

Both on the top and bottom sides, in front part of the weld pool, we can observe vortexes driving the liquid from the hottest area (central part of weld pool, under the arc) to the edges of the weld pool corresponding to colder areas. This is in agreement with the Marangoni force which is often considered as the main force driving fluid flow by gradient of surface tension. The liquid metal is then pushed from the front of the weld pool (fusion line) to the rear.

The increase of the flow velocities with the linear energy is also in accordance with the transport mechanism driven

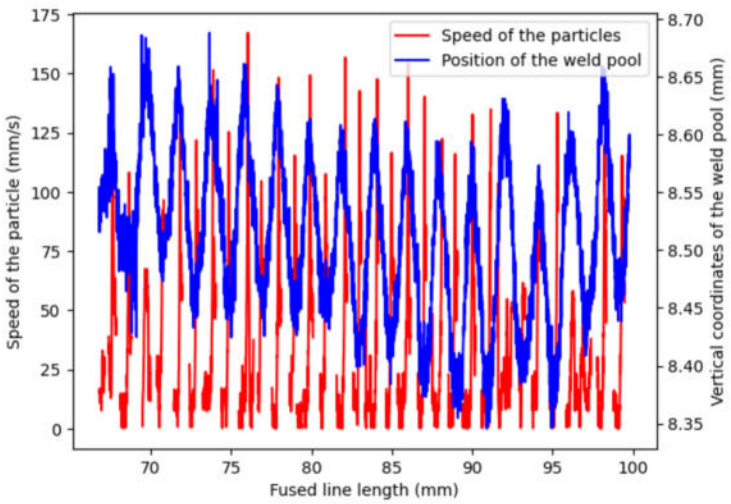

Fig. 10 Position of the center of mass of the liquid metal according to y axis and evolution of the average particle speeds along the weld bead

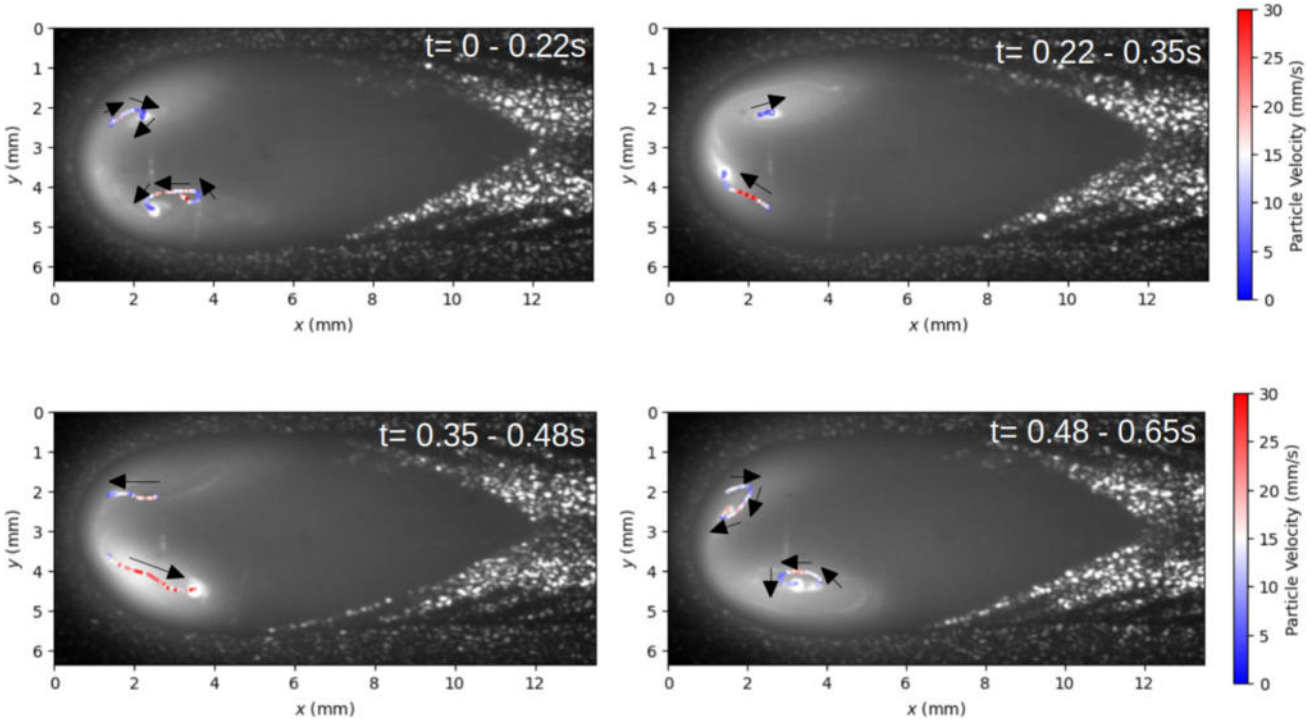

Fig. 11 Example of the oscillating movements and speed of the particles for w_s =3.3 mm/s, bottom side

by the Marangoni effect. In the studied configuration, the Marangoni number $Ma = -\frac{\partial\sigma}{\partial T}\frac{L\Delta T}{\mu\alpha}$, which compares the rate of transport due to surface tension gradient with the rate of transport of diffusion, is directly proportional to the characteristic length L (T is temperature and α thermal diffusivity). This characteristic length which can be assimilated here to the half-width of the weld pool increases with the linear energy, inducing an increase of Ma, in relation with this liquid convection phenomenon.

With the measured liquid velocities, whatever the welding speed configuration, the calculated Reynolds numbers are lower than 1000, indicating that the flows would not be turbulent. However, the velocity values are lower limits obtained by surface measurements that do not necessarily reflect the liquid velocities in the bulk of the weld pool. The similarities of the movements observed both on top and bottom sides and their synchronization suggest roll-like flow in weld pool.

Although we cannot measure the flow going on between the upper and lower sides of the weld pool, apparition of heated zones on the bottom surface indicates that hot liquid coming from the upper side is moving downwards. These zones are always located in the front and side of the molten pool. The Péclet number $Pe_{th} = \frac{uL}{\alpha}$ (with u the fluid flow velocity), which represents the ratio between thermal convection and thermal conduction, is between about 5 and 100 at weld pool scale. These values and the observed fluid flow underline the fact that fluid flows are mainly responsible for heat transfer in the weld pool and from top side to bottom

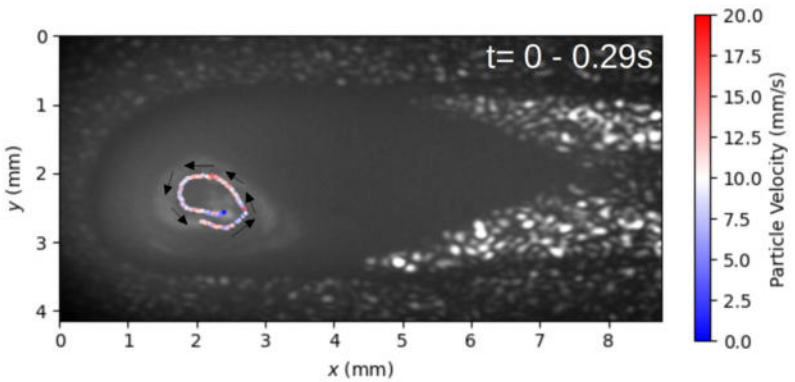

Fig. 12 Movement of the particle following a vortex observed for w_s = 4.3 mm/s, bottom side

side. At the global scale of the weld pool, heat transfer from the front to the rear of the weld pool helps to homogenize temperature and contribute to the global shape of the weld pool.

For two of the studied configurations, the weld pool behavior presents a global oscillatory regime of the liquid metal in the front part of the molten zone, with movements showing an altered feeding from one vortex to another. These observations are done for the two biggest sizes of weld pool, corresponding to highest linear energy, whereas for the smallest weld pool, no oscillatory regime is observed but only an asymmetry of the vortex position. The initiation of this oscillatory regime could come from a perturbation in the system (in relation with heat transfer), leading to a first asymmetry in the fluid flow and creating this instability. Once the oscillation is initiated, one side of the weld pool is more heated than the other due to the concentration of the flow in this area. The Marangoni effect may then drive the fluid located in the vortex zone to colder areas, namely the other side of the weld pool, perpetuating the oscillation. The fact that no oscillation is observed for $w_s = 4.3$ mm/s indicates that the size of the weld pool seems to have a significant effect on the instability initiation, probably by decreasing the influence of the Marangoni effect compared to diffusive one when its size is decreasing. These results demonstrate the appearance of an instability whose controlling parameter is the welding speed. There is a change from the presence of one vortex inside the weld pool to an oscillatory behavior with an increasing frequency. It could be imagined that if the linear heat input is increased, the fluid flow velocity will continue to increase, due to the increase of the weld pool length and to the peak temperature on which Marangoni forces can act. This could lead to the appearance of turbulence inside the weld pool, but as outlined earlier, it will tend to homogenize the temperature.

5 Conclusion

Fluid flow during GTA welding has been investigated with in-situ observations of fully penetrated weld pools. The experimental setup allows the observation of both the upper and the lower sides of the weld pool, and visible fluid flows are described with particle tracking velocimetry. The influence of the increase of linear energy on the size of the weld pool as well as the surface fluid velocities on the lower side has been quantified, and the surface fluid flows have been described. The obtained data can be used as benchmark for numerical simulations. Fluid flow appears to be mainly driven by the Marangoni force, in relation with energy input. An oscillatory behavior was also observed, with vortexes moving from one side to the other side of the weld pool. This behavior is not observed for small weld pools but appears for larger sizes. It could be assimilated to an instability, and further investigations have to be done for a better understanding of the initiation of such a behavior. The analysis that combined measurement of the contour with local velocity measurement demonstrated the importance of the Marangoni effect in this configuration. The results show a correlation between temperature distribution and fluid motion. Nevertheless, despite the high Peclet number, cautions should be taken when discussing the coupling between thermal distribution and fluid flow due to non-free flow conditions with high heat input on the top side that partly drives the temperature distribution.

Supplementary Information The online version contains supplementary material available at https://doi.org/10.1007/s40194-024-01913-3.

Funding This work was funded by the Agence Nationale de la Recherche under the project NEMESIS (ANR-17-CE08-0036) (https://anr.fr/Project-ANR-17-CE08-0036).

Data Availability None.

Declarations

Conflict of interest The authors declare no competing interests.

References

1. Fan HG, Tsai HL, Na S-J (2000) Heat transfer and fluid flow in a partially or fully penetrated weld pool in gas tungsten arc welding. Int J Heat Mass Transfer 44:417–428. https://doi.org/10.1016/S0017-9310(00)00094-6
2. Tanaka M, Lowke JJ (2006) Predictions of weld pool profiles using plasma physics. J Phys D Appl Phys 40(1):1. https://doi.org/10.1088/0022-3727/40/1/R01
3. Wang Y, Tsai HL (2001) Effects of surface active elements on weld pool fluid flow and weld penetration in gas metal arc welding. Metall and Mater Trans B 32:501–515. https://doi.org/10.1007/s11663-001-0035-5
4. Meng X, Qin G, Zou Z (2017) Sensitivity of driving forces on molten pool behavior and defect formation in high-speed gas tungsten arc welding. Int J Heat Mass Transfer 107:1119–1128. https://doi.org/10.1016/j.ijheatmasstransfer.2016.11.025
5. Wu F, Falch KV, Guo D, English P, Drakopoulos M, Mirihanage W (2020) Time evolved force domination in arc weld pools. Mater Des 190:108534. https://doi.org/10.1016/j.matdes.2020.108534
6. Kidess A, Kenjereš S, Kleijn CR (2016) The influence of surfactants on thermocapillary flow instabilities in low Prandtl melting pools. Phys Fluids 28(6):062106. https://doi.org/10.1063/1.4953797
7. Ebrahimi A, Kleijn CR, Hermans MJM, Richardson IM (2021) The effects of process parameters on melt-pool oscillatory behaviour in gas tungsten arc welding. J Phys D Appl Phys 54(27):275303. https://doi.org/10.1088/1361-6463/abf808
8. Chen Y, David SA, Zacharia T, Cremers CJ (1998) Marangoni convection with two free surfaces. Numer Heat Transfer Part A: Appl 33(6):599–620. https://doi.org/10.1080/10407789808913957

9. Traidia A, Roger F (2011) Numerical and experimental study of arc and weld pool behaviour for pulsed current GTA welding. Int J Heat Mass Transfer 54(9):2163–2179. https://doi.org/10.1016/j.ijheatmasstransfer.2010.12.005
10. Wang X, Luo Y, Fan D (2019) Investigation of heat transfer and fluid flow in high current GTA welding by a unified model. Int J Therm Sci 142:20–29. https://doi.org/10.1016/j.ijthermalsci.2019.04.005
11. Zhao C, Steijn V, Richardson I, Saldi Z, Kleijn C (2009) Experimental characterization of GTA weld pool surface flow using PIV. ASM proceedings of the international conference: Trends in welding research, pp 201–210. https://doi.org/10.1361/cp2008twr201
12. Zhao C, Steijn V, Richardson I, Kleijn C, Kenjeres S, Saldi Z (2009) Unsteady interfacial phenomena during inward weld pool flow with an active surface oxide. Sci Technol Weld Join 14:132–140. https://doi.org/10.1179/136217108X370281
13. Chiocca A, Bordreuil C, Soulié F, Deschaux-Beaume F (2019) An analysis of fluid flows and solidification mechanisms during GTA welding by the means of in situ observations. Weld World. https://doi.org/10.1007/s40194-018-0673-8
14. Choo RTC, Szekely J (1994) The possible role of turbulence in GTA weld pool behavior. Weld J 25–31
15. Katayama S, Kawahito Y, Mizutani M (2010) Elucidation of laser welding phenomena and factors affecting weld penetration and welding defects. Phys Proc 5:9–17. https://doi.org/10.1016/j.phpro.2010.08.024. Laser Assisted Net Shape Engineering 6, Proceedings of the LANE 2010, Part 2
16. Wu F, Flint TF, Falch KV, Smith MC, Drakopoulos M, Mirihanage W (2021) Mapping flow evolution in gas tungsten arc weld pools. Int J Heat Mass Transfer 179:121679. https://doi.org/10.1016/j.ijheatmasstransfer.2021.121679
17. Aucott L, Dong HB, Mirihanage W, Atwood R, Kidess A, Gao S, Wen S, Marsden J, Feng S, Tong M, Connolley T, Drakopoulos M, Kleijn C, Richardson I, Browne D, Mathiesen R, Atkinson H (2018) Revealing internal flow behaviour in arc welding and additive manufacturing of metals. Nat Commun 9:. https://doi.org/10.1038/s41467-018-07900-9
18. Nakamura H, Kawahito Y, Nishimoto K, Katayama S (2015) Elucidation of melt flows and spatter formation mechanisms during high power laser welding of pure titanium. J Laser Appl 27(3):032012. https://doi.org/10.2351/1.4922383. https://pubs.aip.org/lia/jla/article-pdf/doi/10.2351/1.4922383/13916383/032012_1_online.pdf
19. Anh NV, Tashiro S, Hanh BV, Tanaka M (2017) Experimental investigation on the weld pool formation process in plasma keyhole arc welding. J Phys D Appl Phys 51(1):015204. https://doi.org/10.1088/1361-6463/aa9902
20. Pichler P, Simonds B, Sowards J, Pottlacher G (2020) Measurements of thermophysical properties of solid and liquid NIST SRM 316l stainless steel. J Mater Sci 55:. https://doi.org/10.1007/s10853-019-04261-6
21. Brooks R, Quested P (2005) The surface tension of steels. J Mater Sci 40:2233–2238. https://doi.org/10.1007/s10853-005-1939-2
22. Mills K, Su Y, Li Z, Brooks R (2004) Equations for the calculation of the thermophysical properties of stainless steel. Isij Int 44:1661–1668. https://doi.org/10.2355/isijinternational.44.1661
23. Romero E, Chapuis J, Bordreuil C, Soulié F, Fras G (2013) Image processing and geometrical analysis for profile detection during pulsed gas metal arc welding. Proc Inst Mech Eng Part B J Eng Manuf 227(3):396–406. https://doi.org/10.1177/0954405412470420
24. Allan D, Wel C, Keim N, Caswell TA, Wieker D, Verweij R, Reid C, Thierry Grueter L, Ramos K, Apiszcz Z, Perry RW, Boulogne F, Sinha P, Pfigliozzi BN, Uieda L, Katins J, Mary H, Ahmadia A (2019) Soft-matter/trackpy: Trackpy V0.4.2. https://doi.org/10.5281/zenodo.3492186
25. Chiocca A (2016) Etude de l'influence des écoulements dans le bain de fusion sur les mécanismes de solidification en soudage sur l'alliage cu30ni. PhD thesis. Thèse de doctorat dirigée par Frédéric Deschaux-Beaume, Laboratoire de Mécanique et Génie Civil, Montpellier 2016. http://www.theses.fr/2016MONTT312/document